HAL
open science

SCUBA observations of the Horsehead Nebula - what did the horse swallow?

D. Ward-Thompson, D. Nutter, Sylvain Bontemps, A. Whitworth, R. Attwood

To cite this version:

D. Ward-Thompson, D. Nutter, Sylvain Bontemps, A. Whitworth, R. Attwood. SCUBA observations of the Horsehead Nebula - what did the horse swallow?. Monthly Notices of the Royal Astronomical Society, 2006, 369 (3), pp.1201-1210. 10.1111/j.1365-2966.2006.10356.x . hal-00109397

HAL Id: hal-00109397

https://hal.science/hal-00109397v1

Submitted on 17 Mar 2021

HAL is a multi-disciplinary open access archive for the deposit and dissemination of scientific research documents, whether they are published or not. The documents may come from teaching and research institutions in France or abroad, or from public or private research centers.

L'archive ouverte pluridisciplinaire **HAL**, est destinée au dépôt et à la diffusion de documents scientifiques de niveau recherche, publiés ou non, émanant des établissements d'enseignement et de recherche français ou étrangers, des laboratoires publics ou privés.

Mon. Not. R. Astron. Soc. **369,** 1201–1210 (2006) doi:10.1111/j.1365-2966.2006.10356.x

SCUBA observations of the Horsehead nebula – what did the horse swallow?

D. Ward-Thompson,[1,2]★ D. Nutter,[1] S. Bontemps,[2] A. Whitworth[1] and R. Attwood[1]

[1]*Department of Physics and Astronomy, Cardiff University, 5 The Parade, Cardiff CF24 3YB*
[2]*Observatoire de Bordeaux, 2 rue de l'Observatoire, 33270 Floirac, France*

Accepted 2006 March 21; received 2006 March 20; in original form 2005 December 6

Downloaded from https://academic.oup.com/mnras/article/369/3/1201/1229160 by guest on 17 March 2021

ABSTRACT

We present observations taken with the Submillimetre Common-User Bolometer Array (SCUBA) on the James Clerk Maxwell Telescope (JCMT) of the Horsehead nebula in Orion (B33), at wavelengths of 450 and 850 μm. We see bright emission from that part of the cloud associated with the photon-dominated region (PDR) at the 'top' of the horse's head, which we label B33-SMM1. We characterize the physical parameters of the extended dust responsible for this emission, and find that B33-SMM1 contains a more dense core than was previously suspected, with a mass of $\sim 2\,M_\odot$ in a region of 0.31×0.13 pc, and a peak volume density of $\sim 6 \times 10^5\,cm^{-3}$. We compare the SCUBA data with data from the *Infrared Space Observatory* (*ISO*) and find that the emission at 6.75 μm is offset towards the west, indicating that the mid-infrared emission is tracing the PDR while the submillimetre emission comes from the molecular cloud core behind the PDR. We calculate the virial balance of this core and find that it is not gravitationally bound but is being confined by the external pressure from the H II region IC434, and that it will either be destroyed by the ionizing radiation, or else may undergo triggered star formation.

Furthermore, we find evidence for a lozenge-shaped clump in the 'throat' of the horse, which is not seen in emission at shorter wavelengths. We label this source B33-SMM2 and find that it is brighter at submillimetre wavelengths than B33-SMM1. We calculate the physical parameters of SMM2 and find it has a mass of $\sim 4\,M_\odot$ in a region 0.15×0.07 pc, with a peak volume density of $\sim 2 \times 10^6\,cm^{-3}$ and peak column density of $\sim 9 \times 10^{22}\,cm^{-2}$. SMM2 is seen in absorption in the 6.75-μm *ISO* data, from which we obtain an independent estimate of the column density in excellent agreement with that calculated from the submillimetre emission. We calculate the stability of this core against collapse and find that it is in approximate gravitational virial equilibrium. This is consistent with it being a pre-existing core in B33, possibly pre-stellar in nature, but that it may also eventually undergo collapse under the effects of the H II region.

Key words: stars: formation – ISM: clouds – ISM: individual: B33 – ISM: individual: Horsehead nebula – submillimetre.

1 INTRODUCTION

The Horsehead nebula in Orion is one of the most familiar images in astronomy – see Fig. 1. It appears as B33 in the catalogue of dark clouds of Barnard (1919). It has been observed by many people at many wavelengths. Recent studies by Pound, Reipurth & Bally (2003), Abergel et al. (2003), Teyssier et al. (2004), Pety et al. (2005) and Habart et al. (2005) have concentrated on the edge of the nebula that is nearest to the H II region (the 'top' of the horse's head). All derived various values for the gas densities and temperatures across the photon-dominated region (PDR) that exists along this edge of the nebula.

Abergel et al. (2003) confirmed that the star σ Orionis is responsible for the ionizing radiation producing the PDR. They deduced that the PDR is ~ 0.01 pc in thickness and they found densities of $\sim 10^4\,cm^{-3}$ immediately behind the ionization front. Teyssier et al. (2004) presented observations of various carbon-bearing species, and Pety et al. (2005) showed interferometer observations of the PDR from which they concluded that no current model of PDRs

★E-mail: Derek.Ward-Thompson@astro.cf.ac.uk

© 2006 The Authors. Journal compilation © 2006 RAS

Figure 1. Optical image of the Horsehead nebula taken with the Very Large Telescope. West is towards the top, north is to the left-hand side. Image courtesy of the European Southern Observatory (ESO).

could explain all of their data, and that this might be explained by fragmentation of polycyclic aromatic hydrocarbon (PAH) molecules by the intense ultraviolet field. Habart et al. (2005) found very bright, narrow filaments of fluorescent H_2 emission along the edge of the PDR. Hily-Blant et al. (2005) studied the velocities across the nebula as a whole and found a complex series of helical rotational velocity gradients.

Pound et al. (2003) asserted that the Horsehead nebula is an extension of the L1630 dark cloud, seen against the background H II region IC434, illuminated edge-on by the O9.5V star σ Orionis. They compared the nebula to the now equally famous Eagle nebula with its 'pillars' of gas and dust. They deduced that the two nebulae were formed in a somewhat similar fashion, by the action of nearby massive stars and their associated H II regions, either by an instability or an ionization front. Williams, Ward-Thompson & Whitworth (2001) argued that the formation of such 'pillars' or 'columns' of dust and gas is probably a fairly common phenomenon in star formation.

One difference between the Eagle nebula and the Horsehead nebula is that whereas dense condensations have been known for some time to exist in the pillars of the Eagle nebula (e.g. White et al. 1999), until recently no similar condensations were known in the Horsehead nebula. These dense condensations are the likely progenitors of the next generation of star formation and may give clues as to the initial conditions for star formation in such regions. Studies of these dense clumps may therefore provide indicators that will allow us to differentiate between the various models of 'triggered' and 'spontaneous' star formation (e.g. Ward-Thompson et al. 2006).

In this paper, we present submillimetre continuum data of the Horsehead nebula, retrieved from the James Clerk Maxwell Telescope (JCMT) data archive, taken by the Submillimetre Common-User Bolometer Array (SCUBA). Our goal in obtaining the data was to search for condensations in the densest parts of the Horsehead nebula, to see whether future star formation is likely in this region, before it is possibly destroyed in $\sim 5 \times 10^6$ yr, as estimated by Pound et al. (2003).

2 DATA

The data were obtained from the JCMT data archive. This source has been observed several times by SCUBA. Only those data with the highest signal-to-noise ratio were used to make maps of the region at 850 and 450 μm. These were taken in 1999 November 30 at 02:49–04:35 h *HST* (UT 12:49–14:35). Data were taken at both wavelengths simultaneously using SCUBA in its standard on-the-fly mapping mode (Holland et al. 1999). Average sky conditions during the observations were determined using the 'skydip' method and by comparison with the 1.3-mm sky opacity. The 1.3-mm optical depth ranged from 0.033 to 0.035 during the observations. The 850-μm zenith optical depth was 0.117–0.123 corresponding to a mean zenith transmission of ∼90 per cent. The 450-μm optical depth was 0.50–0.54 corresponding to a zenith transmission of ∼60 per cent.

The data were reduced in the normal way using the SCUBA User Reduction Facility (Jenness & Lightfoot 2000). Calibration was performed using observations of the planet Mars. We estimate that the absolute calibration uncertainty is ±10 per cent at 850 μm and ±25 per cent at 450 μm, based on the consistency and reproducibility of the calibration. The average beam size full width at half-maximum (FWHM) was found to be 15 arcsec at 850 μm and 10 arcsec at 450 μm. These numbers are both slightly higher than the notional beamwidths at these wavelengths. Fitting two-component Gaussians to the calibrator source showed there to be a negligible error beam at 850 μm, but at 450 μm a significant error beam was detected that was found to contribute up to 10 per cent of the flux density. This was taken into account in calibrating the data by using identical apertures when determining the calibration on the planet Mars and measuring the flux densities of the sources. In the final maps, it was found that the average 1σ noise (off-source) was 17 mJy beam^{-1} at 850 μm and 110 mJy beam^{-1} at 450 μm.

Fig. 2 shows the 850-μm data of the region, rotated to the same orientation as the optical image in Fig. 1. The outline of the horse's head can be clearly seen in this image. In addition, a brighter region along the 'top' of the horse's head can be seen, roughly coincident with the PDR discussed in Section 1 above, which we here label B33-SMM1. However, we also see a second bright source in the image, in the area of the horse's 'throat', looking just as if the horse has swallowed a large lump. We here label this source B33-SMM2.

Fig. 3 shows the 450-μm image of the same region. The signal-to-noise ratio of this image is not as high as that of the 850-μm image. None the less the approximate outline of the nebula can still be seen. Once again the source near the PDR is visible – SMM1. The source in the horse's throat can also be seen in this image – SMM2.

Table 1 lists the measured parameters of SMM1 and 2. We quote the central positions and sizes of the two sources. The size of each source was calculated by fitting the elliptical aperture that most closely matched the 3σ contour enclosing each source. The flux densities in these apertures were measured at 850 and 450 μm and are listed in Table 1, along with the peak flux density of each source. We see from Table 1 that SMM1 is the more extended of the two sources, although SMM2 is the brighter of the two, as its peak flux density is greater at both wavelengths. Furthermore, even though SMM2 is the more compact source, its extended flux

Downloaded from https://academic.oup.com/mnras/article/369/3/1201/1229160 by guest on 17 March 2021

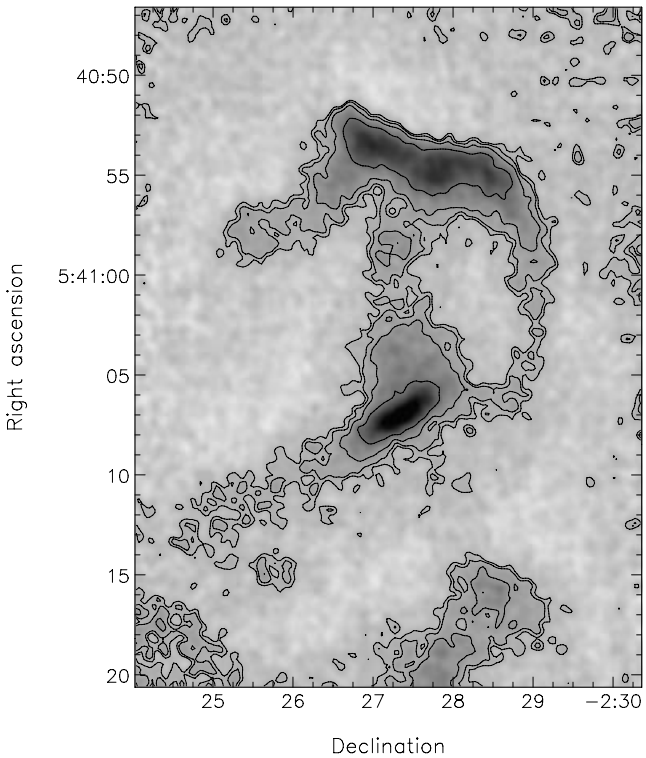

Figure 2. SCUBA 850-μm image of the Horsehead nebula. The region shown is approximately the same as that in Fig. 1. West is towards the top, north is to the left-hand side. Contour levels are at 2, 3, 5 and 10σ, where 1σ is 17 mJy beam^{-1}. The FWHM beam size is 15 arcsec. The familiar Horsehead shape can be seen in this image, as well as the source SMM1 associated with the PDR along the 'top' of the horse's head, and the source SMM2 in the horse's 'throat'.

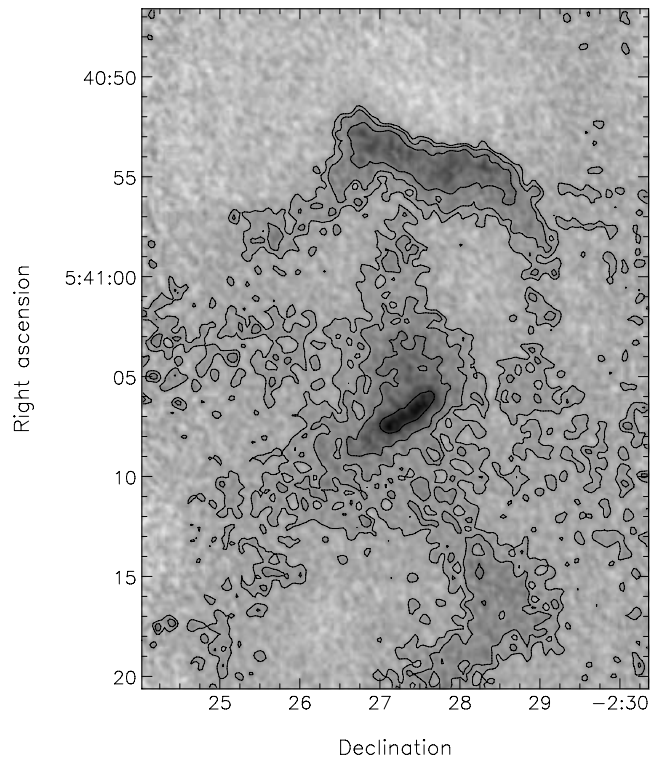

Figure 3. SCUBA 450-μm image of the Horsehead nebula. The same region is shown as in Fig. 2 and in the same orientation. Contour levels are again at 2, 3, 5 and 10σ, where 1σ is now 110 mJy beam^{-1}. The FWHM beam size is 10 arcsec. The signal-to-noise ratio is lower than in the 850-μm image, although the horse's head shape can still be made out. Once again the source associated with the PDR, SMM1, and the source in the throat, SMM2, can be seen.

density is greater at 450 μm than SMM1, and it is comparable at 850 μm.

SMM1 appears to run roughly along the full length of the ridge of the PDR that has been extensively studied recently (e.g. Habart et al. 2005, and references therein). To check how well the extent of the submillimetre emission along the ridge matches the mid-infrared emission from this source, as seen by the *Infrared Space Observatory* (*ISO*) using the ISOCAM mid-infrared camera, we compared the two data sets in more detail.

Fig. 4 shows once again the contours of 850-μm emission from Fig. 2, but this time these are plotted over a grey-scale of the 6.75-μm emission seen by ISOCAM (cf. Abergel et al. 2003). We see from this plot that the mid-infrared emission lies along the western edge of the 850-μm emission from SMM1. The infrared ridge is offset from the submillimetre ridge by ∼20–25 arcsec. This is as expected, given that the cloud is being externally heated by σ Ori (e.g. Pound et al. 2003).

The warmer dust on the side of the cloud nearest to the heating source emits more strongly in the mid-infrared, while the cooler dust further into the cloud emits at longer wavelengths. In fact the mid-infrared emission appears to wrap right round the outside of the cloud, exactly as expected for such an outside-in temperature gradient (cf. Ward-Thompson, André & Kirk 2002). In fact, the 850-μm emission matches better the molecular line emission traced by various isotopomers of CO (cf. Abergel et al. 2003; Habart et al. 2005).

SMM1 was seen as two separate sources by Johnstone, Matthews & Mitchell (2006), who used an automated source-finding procedure to locate all of the sources detected by SCUBA in the Orion region. We see SMM1 as simply an undulating ridge, as we do not

Table 1. Positions and sizes, together with peak and integrated flux densities (quoted to three significant figures), of the two submillimetre sources B33-SMM1 and 2. The peak flux densities are quoted in a single beam, which was measured to be 15 arcsec at 850 μm and 10 arcsec at 450 μm. The integrated flux densities were measured within the apertures quoted. The 1σ error bars on the peak flux densities are 17 and 110 mJy beam^{-1} at 850 and 450 μm, respectively. The absolute error bars are estimated to be ±10 per cent and ±25 per cent at 850 and 450 μm, respectively. The aperture sizes were defined by the best-fitting ellipse to the 3σ contour level enclosing each source. The major and minor axes of the ellipse are quoted, together with the position angle of the major axis, measured north through east.

Source	Right ascension (2000)	Declination (2000)	$S_{850}^{\rm peak}$ (mJy beam^{-1})	$S_{850}^{\rm int}$ (mJy)	$S_{450}^{\rm peak}$ (mJy beam^{-1})	$S_{450}^{\rm int}$ (mJy)	Aperture (arcsec) (major × minor)	Position angle (N → E)
B33-SMM1	$05^{\rm h}\,40^{\rm m}\,54^{\rm s}$	−02° 27′ 32″	280	1470	1050	6570	161 × 68	160°
B33-SMM2	$05^{\rm m}\,41^{\rm m}\,07^{\rm s}$	−02° 27′ 21″	430	1380	1550	10 300	78 × 36	38°

Downloaded from https://academic.oup.com/mnras/article/369/3/1201/1229160 by guest on 17 March 2021

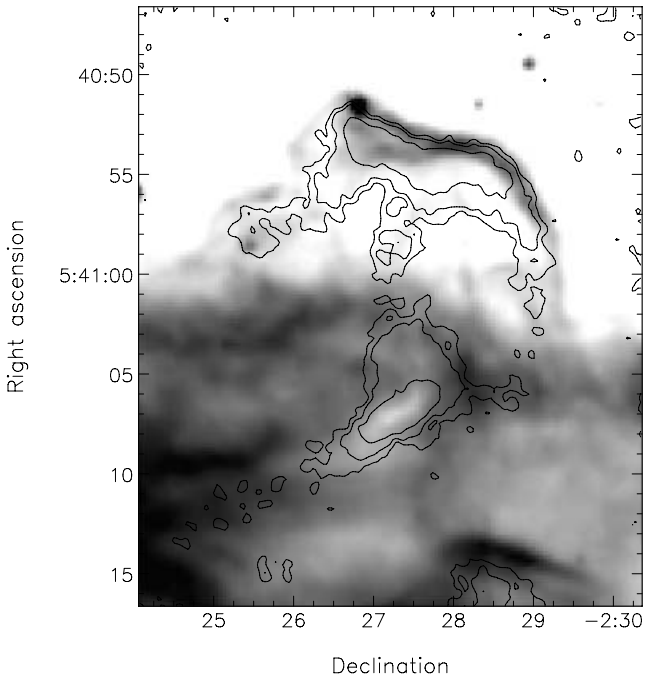

Figure 4. SCUBA 850-μm isophotal contour map of the Horsehead nebula overlaid on a grey-scale of the ISOCAM 6.75-μm image. The region shown is the same as that in Fig. 2. West is towards the top, north is to the left-hand side. Contour levels are as in Fig. 2. The submillimetre emission from the source SMM1 can now be seen to be offset from the infrared emission, with the latter lying closer to the H II region and appearing almost to wrap around the submillimetre source. The source SMM2 in the horse's throat can be seen to be associated with a dip in the mid-infrared emission (cf. Abergel et al. 2003).

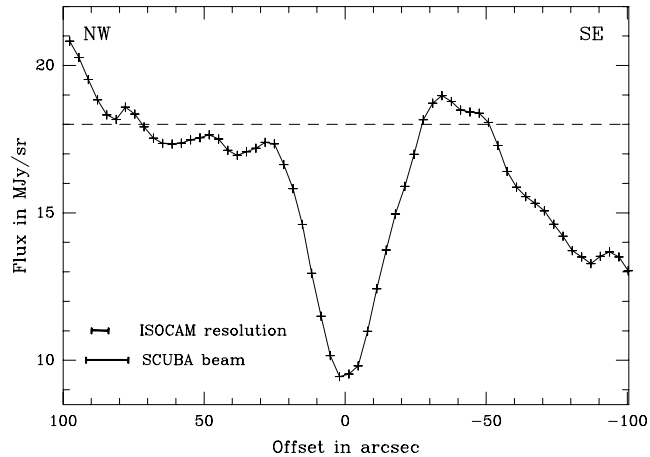

Figure 5. One-dimensional cut of the 6.75-μm map shown in Fig. 4 through the central position of SMM2, orthogonal to its long axis. The *x*-axis is marked in arcsec offset from SMM2, with the north-westerly direction marked as positive. The *y*-axis is labelled in units of MJy sr^{-1}. A clear absorption trough can be seen at the position of SMM2. The horizontal dashed line is a fit to the extended emission of the cloud away from SMM2.

see evidence for strongly peaked sources within the ridge. This is perhaps a matter of interpretation, although we have found in the past that automated routines sometimes tend to extract multiple sources in the presence of a ridge of emission (Nutter 2004).

SMM2 was seen in the 1.2-mm continuum data taken with the 30-m telescope of the Institut de Radio Astronomie Millimétrique (IRAM) at 11-arcsec resolution, as reported by Teyssier et al. (2004) and Habart et al. (2005), although neither of these teams discussed this source in particular. We see a broad match between the IRAM data and the SCUBA data, which are consistent given the different angular resolutions and noise levels of the different data sets.

SMM2 also overlaps with 'peak 2' in the $C^{18}O$ ($J = 2 \rightarrow 1$) data of Hily-Blant et al. (2005), although there is an offset of ∼17 arcsec between the peak positions of our SMM2 and their peak 2. Our 850-μm peak position coincides better with the 1.2-mm peak of Teyssier et al. (2004). This offset is explained by Hily-Blant et al. (2005) as being caused by depletion. Their peak 1 appears to have been detected in our data, and the positions of their peaks 3 and 4 show some 850-μm dust emission in our data, but nothing significantly above the general extended emission of the nebula. This may be indicating that these latter 'peaks' may simply be generated by optical depth effects in $C^{18}O$.

Johnstone et al. (2006) also detected SMM2 at 850 μm, and our measured peak flux densities of both SMM1 and 2 are in good agreement with theirs, so we believe that our flux density calibration is good. None the less, we find slightly different extended flux densities in both cases (even allowing for their two sources in SMM1). Johnstone et al. (2006) used a complex method to estimate extended flux densities, that entailed smoothing the data to 130 arcsec and subtracting this smoothed image. Then they added back a constant offset to zero the areas of no emission, and they used an automated routine to choose their aperture sizes.

We repeated their technique, and could only reproduce their measured extended flux densities by using an aperture that included what we believe to be flux from the extended cloud as well as from the cores. Based on our examination of the data, we believe our apertures to be a good fit to the source in each case. Johnstone et al. (2006) do not discuss the nature of SMM1 and 2 in particular, merely treating them as part of their statistical study of clumps in the Orion region in general.

SMM2 has not previously been observed in any shorter wavelength observations. However, close examination of the ISOCAM data in Fig. 4 shows that there appears to be a dip in the emission at the position of SMM2 (cf. Abergel et al. 2003). We believe this could be due to absorption of this background emission by the dense core of SMM2. This dip was also noted by Hily-Blant et al. (2005) and associated with their peak 2, although it aligns much better with the submillimetre source SMM2.

Fig. 5 shows a one-dimensional cut of the mid-infrared grey-scale shown in Fig. 4 through the centre of SMM2. The cut was made along an axis orthogonal to the long axis of SMM2. There is clearly structure associated with the cloud as a whole. There is possibly a gradient from north-west to south-east that can be seen at the extremes of the cut. However, there is also a very clear absorption 'trough' exactly at the position of SMM2. The horizontal dashed line is an estimate of the cloud emission away from SMM2, where it appears roughly constant. We return to this in Section 3.2 below, where we use the depth of the trough to obtain an independent estimate of the column density of SMM2.

3 MASSES AND DENSITIES

We can use the parameters we have measured for SMM1 and 2, together with those measured in previous work, to derive the physical conditions within the two sources. Adopting the canonical distance of 400 pc for the Horsehead nebula (see e.g. discussion in Pound et al. 2003), we can calculate the actual sizes of the sources SMM1 and 2. These are listed in Table 2. We now treat each source in turn.

Downloaded from https://academic.oup.com/mnras/article/369/3/1201/1229160 by guest on 17 March 2021

Table 2. Masses and densities derived for B33-SMM1 and 2. The distance adopted is 400 pc. The justifications for the adopted distance and dust temperatures T are given in the text. Given the assumptions in the mass calculations, the uncertainties on masses and densities could be a factor of the order of a few (see text for discussion). Therefore, the masses and densities are only quoted to one significant figure. The mean column densities $\overline{N}(H_2)$ and volume densities $\overline{n}(H_2)$ throughout the whole source are quoted, calculated from the integrated flux densities. The peak column densities $N(H_2)_{peak}$ and volume densities $n(H_2)_{peak}$ are also quoted, as calculated from the peak flux densities.

Source	Distance (pc)	Size (pc)	T (K)	Mass ($M_\odot$)	$\overline{N}(H_2)$ (cm^{-2})	$\overline{n}(H_2)$ (cm^{-3})	$N(H_2)_{peak}$ (cm^{-2})	$n(H_2)_{peak}$ (cm^{-3})
B33-SMM1	400	0.31×0.13	22	2	4×10^{21}	1×10^4	4×10^{22}	6×10^5
B33-SMM2	400	0.15×0.07	15	4	3×10^{22}	1×10^5	9×10^{22}	2×10^6

3.1 B33-SMM1

Fig. 4 shows how the ISOCAM 6.75-μm emission (Abergel et al. 2003) traces the edge of the molecular cloud core SMM1 nearest to the H II region. As mentioned above, the length of SMM1 is roughly comparable to the ISOCAM data, although we now see that the width of the submillimetre source (0.13 pc) is much greater than the width of the ISOCAM filament (0.01 pc). We interpreted this above as a temperature gradient across the cloud, with the warmer infrared-emitting dust seen along the edge (which may be due to small grains or PAHs), while the cooler dust extends deeper into the cloud. Our submillimetre dust emission appears to match the CO emission of Abergel et al. (2003) more closely than the mid-infrared ISOCAM emission. Abergel et al. (2003) derive a kinetic temperature of 30–40 K for the PDR.

A similar temperature gradient effect is seen by Habart et al. (2005), who find (from model calculations) a kinetic temperature of 22 K at a depth of 0.02 pc into the cloud with gas at a volume density of 2×10^4 cm^{-3}, and 13.5 K at a volume density of 2×10^5 cm^{-3}. We can calculate the mass of gas and dust responsible for emission in our two submillimetre sources from the 850-μm flux densities, using various assumptions, provided we know the temperature of the emitting dust. This is because submillimetre continuum emission is usually optically thin, and hence it is a direct tracer of the mass content of molecular cloud cores (cf. Kirk, Ward-Thompson & André 2005).

For a spherical isothermal dust source at distance d, the total (dust plus gas) mass, $M(r < R)$, contained within a radius R from the centre, is related to the submillimetre flux density $S_{850\,\mu m}(\theta)$ integrated over a circle of projected angular radius $\theta = R/d$ by the equation

$$M(r < R) = \frac{S_{850\,\mu m}(\theta)\, d^2}{\kappa_{850}\, B_{850}(T)}, \qquad (1)$$

where κ_{850} is the dust opacity per unit mass column density at $\lambda = 850$ μm and $B_{850}(T)$ is the Planck function at the same wavelength, for a dust temperature T.

For the dust opacity, we follow the method adopted by André, Ward-Thompson & Motte (1996) and subsequently used by Kirk et al. (2005), and use $\kappa_{850} = 0.01\,cm^2\,g^{-1}$ (see André, Ward-Thompson & Barsony 1993; André et al. 1996; Ward-Thompson, Motte & André 1999; for detailed justifications both of this value of κ_{850} in particular and this method of obtaining masses in general). The uncertainties in the masses due to a combination of uncertainties in κ could be as high as a factor of a few (see André et al. 1996).

For SMM1 we have a range of temperatures which we could adopt, as discussed above, given that there is probably a temperature gradient across the source. As stated above, Habart et al. (2005) found in their model that a mean density of 2×10^4 cm^{-3} yields a temperature of 22 K, while a mean density of 2×10^5 cm^{-3} gives a temperature of 13.5 K. At these temperatures, the masses derived from submillimetre continuum data are very sensitive to temperature, due to the exponential nature of the Planck function.

Adopting a temperature of 22 K gives us a mass for SMM1 of $\sim 2\,M_\odot$, while a temperature of 13.5 K gives a mass of $\sim 4\,M_\odot$. We can check for internal consistency by calculating a mean density for SMM1 based on each of these masses in turn. To do this, we need to assume the line-of-sight dimension of SMM1. Abergel et al. (2003) treat it as an edge-on plane, whilst Habart et al. (2005) opt for something that is in fact prolate and filamentary in nature. Hence, we take the average of the two and assume that the line-of-sight thickness of SMM1 is the mean of its other two dimensions. Then a mass of $2\,M_\odot$ ($T = 22$ K) yields a mean volume number density of $n(H_2) \sim 1 \times 10^4$ cm^{-3}, and a mass of $4\,M_\odot$ ($T = 13.5$ K) yields a mean volume number density of $n(H_2) \sim 2 \times 10^4$ cm^{-3}.

Hence, we see that a temperature of 13.5 K and a mass of $4\,M_\odot$, yields a mean volume density of 2×10^4 cm^{-3}, compared to the 2×10^5 cm^{-3} used by the model to calculate the temperature of 13.5 K in the first place. Thus, this assumption does not yield a self-consistent result. We note that our line-of-sight assumption only alters these numbers by a factor of $\sim$2, rather than the order-of-magnitude required.

On the other hand, we see that a temperature of 22 K and a mass of $2\,M_\odot$, yields a mean volume density of 1×10^4 cm^{-3}, which is about equal to the mean density used by Habart et al. (2005) to calculate the kinetic temperature of 22 K in the first place, and the calculation is self-consistent. This is also consistent with the mean volume density derived by Abergel et al. (2003). Thus, the whole derivation is self-consistent and consistent with previous work, so these are the values we adopt for SMM1, and we list them in Table 2. We note that Johnstone et al. (2005) assume a Bonnor–Ebert form for this source and find a temperature of 19 K, in reasonable agreement with our adopted value. We also note that the uncertainties on these numbers could therefore be a factor of the order a few, so we only quote masses and densities to one significant figure.

The mean column density we derive for the molecular cloud associated with SMM1 is 4×10^{21} cm^{-2}, which is somewhat higher than the values derived by Abergel et al. (2003) from their CO data. However, these latter authors noted that their derived column density was clearly a lower limit, and only valid for the cloud edge, since they acknowledged that their CO data were almost certainly optically thick in the cloud core.

The peak column density we derive is a factor of 10 higher than the mean column density, and corresponds to the densest part of SMM1. The peak volume density we derive is 6×10^5 cm^{-3}, although we note a larger uncertainty in this number due to the unknown line-of-sight depth of the dense peak region (once again we have assumed that the line-of-sight dimension of the source is the mean of its other

Downloaded from https://academic.oup.com/mnras/article/369/3/1201/1229160 by guest on 17 March 2021

two dimensions). None the less, this is comparable to the densities seen in pre-stellar cores (Kirk et al. 2005), which are dense cores on their way to forming stars (Ward-Thompson et al. 1994). Hence SMM1 may be pre-stellar in nature, and we discuss this possibility in Section 5 below.

3.2 B33-SMM2

The source that we refer to as B33-SMM2 has been detected before at a wavelength of 1.2 mm (Teyssier et al. 2004; Habart et al. 2005), and also at 850 μm (Johnstone et al. 2005). However, most authors have not paid it much attention. It can also be seen as a minor peak in the CO (3–2) data (Habart et al. 2005), although again these authors concentrated primarily on the PDR rather than other structure in the maps. Hily-Blant et al. (2005) labelled a nearby CO source as 'peak 2' in their data, as mentioned in Section 2 above, but it is not clear that these are physically the same source, due to this offset.

There is no shorter wavelength emission detected from SMM2 than our 450-μm data in Fig. 3. In this regard, it is similar to a pre-stellar core (Ward-Thompson et al. 1994) or a Class 0 protostar (André et al. 1993). However, the lack of any known outflow emission from this region appears to rule out the latter scenario.

We can calculate the physical parameters of SMM2 in a similar manner to those we calculated for SMM1. However, once again a large source of uncertainty is the dust temperature T within the source. We note that in projection it is significantly further from the H II region than SMM1 and is most probably shielded by the bulk of the B33 molecular cloud, including SMM1. Therefore SMM2 must be cooler than SMM1, although no previous temperature has been derived for it, since all molecular line tracers so far observed either do not detect it, or are depleted or optically thick in this sightline.

Hence, the 22 K we adopt for SMM1 is clearly too high for SMM2. We noted above the similarity of SMM2 to pre-stellar cores in its extent and appearance (Kirk et al. 2005). Pre-stellar cores have typical temperatures around 10 K (Ward-Thompson et al. 2002). However, we note that none of the cores in this latter study were in the Orion region. Most were in Taurus or Ophiuchus, which are more quiescent regions, and thus 10 K may be too low for SMM2.

So, we have a range of possible temperatures of ∼10–20 K. Therefore, we adopt a temperature of 15 K for SMM2, with an error bar of 5 K. Johnstone et al. (2006) used a Bonnor–Ebert fit to SMM2 and found a temperature of 16 K, in good agreement with our chosen value. We note that if the temperature were 20 K the derived mass and densities would decrease by a factor of 2, and if the temperature were 10 K the mass and densities would increase by a factor of 1.75.

We derive a mass of 4 $M_\odot$ for SMM2, based on this temperature. Given that SMM2 is smaller in extent than SMM1, but with higher mass, it is also therefore more dense. The mean column density is an order of magnitude higher than SMM1, as is the mean volume density. Note that this difference in densities between SMM1 and 2 cannot be accounted for simply by our choice of temperatures for the cores – this can account for at most a factor of 2 rather than an order of magnitude. The peak volume and column densities are also seen to be a factor of ∼2–3 higher in SMM2 than SMM1.

However, our calculated mean column density of SMM2 is in very good agreement with the 3.5×10^{22} cm^{-3} derived for 'peak 2' by Hily-Blant et al. (2005), indicating that their peak 2 may in fact be associated with the extended emission from SMM2. We note that to calculate the mean volume density we have again assumed that the line-of-sight dimension is the mean of the other two. Hily-Blant et al. (2005) assumed a cylindrical geometry and found a mean volume density roughly a factor of 2 lower. But they do not see the high peak values in their $C^{18}O$ data that we see in the dust continuum. If peak 2 and SMM2 are the same, then this may be due to optical depth effects in the CO data, or to gas depletion onto grains at the highest densities, as they surmised.

We have an independent method of checking our column density estimate for SMM2, since as we showed in Fig. 5 above, SMM2 is seen as an absorption dip against the bright background emission of L1630 in the mid-infrared data (cf. fig. 2 of Abergel et al. 2003). From this, we can measure the depth of the absorption at 6.75 and 15 μm, and hence calculate the peak column density of SMM2, following the method of Bacmann et al. (2000).

In this method, one compares the intensity of the emission measured at some position in the general cloud emission that is away from the core, $I_{\rm off}$, with the intensity of the emission measured on the core, $I_{\rm on}$. $I_{\rm off}$ is made up of the sum of the background emission intensity, $I_{\rm back}$, from the illuminating source behind the dense core – in this case from L1630 (Pound et al. 2003) – and the widespread general foreground emission intensity, $I_{\rm fore}$, that includes Zodiacal emission and general Galactic emission on scales larger than the cloud in question. $I_{\rm on}$ is then simply the sum of the foreground emission intensity and the attenuated background emission intensity (Bacmann et al. 2000).

So we have

$$I_{\rm off} = I_{\rm back} + I_{\rm fore} \tag{2}$$

and

$$I_{\rm on} = I_{\rm back}(\mathrm{e}^{-\tau_\lambda}) + I_{\rm fore}, \tag{3}$$

where τ_λ is the optical depth at wavelength λ. Rearranging for τ_λ gives

$$\mathrm{e}^{-\tau_\lambda} = \frac{I_{\rm on} - I_{\rm fore}}{I_{\rm off} - I_{\rm fore}}, \tag{4}$$

and we estimate $I_{\rm fore}$ on a region of the data away from the L1630 cloud emission. There is some uncertainty in the estimate of $I_{\rm fore}$, since it may vary slightly from one part of the map to another, and this may be our chief source of measurement error. We attempted to estimate this by looking at the maximum variation in intensity across the cloud itself, as well as on regions away from the cloud, and used this to calculate our errors.

The optical depth can be converted into a column density via the dust opacity σ_λ, using $N(\mathrm{H_2}) = \tau_\lambda/\sigma_\lambda$. We used $\sigma_{6.75\,\mu\mathrm{m}} = 1.2 \times 10^{-23}$ cm^2 and $\sigma_{15\,\mu\mathrm{m}} = 1.6 \times 10^{-23}$ cm^2 (Bacmann et al. 2000).

For the 6.75-μm data we measured $I_{\rm off} = 18 \pm 0.3$ MJy sr^{-1}, $I_{\rm on} = 9.8 \pm 0.1$ MJy sr^{-1} and $I_{\rm fore} = 5.5 \pm 0.2$ MJy sr^{-1}, yielding $\tau_{6.75\,\mu\mathrm{m}} = 1.07 \pm 0.11$. For the 15-μm data we measured $I_{\rm off} = 36 \pm 0.5$ MJy sr^{-1}, $I_{\rm on} = 27.5 \pm 0.1$ MJy sr^{-1} and $I_{\rm fore} = 25 \pm 0.5$ MJy sr^{-1}, yielding $\tau_{15\,\mu\mathrm{m}} = 1.48 \pm 0.34$.

Therefore, the 6.75-μm data give $N(\mathrm{H_2}) = 8.9 \pm 0.9 \times 10^{22}$ cm^{-2}, and the 15-μm data give $N(\mathrm{H_2}) = 9.3 \pm 2.1 \times 10^{22}$ cm^{-2}. Both estimates are in excellent agreement with our value of peak column density for SMM2 in Table 2 of $N(\mathrm{H_2}) = 9 \times 10^{22}$ cm^{-2}. We note that no temperature estimate is required in this calculation. This gives us added confidence in the parameters for SMM2 that we have calculated from the submillimetre data.

4 DISCUSSION

We can compare the 850- and 450-μm data by calculating the ratio of the emission at these two wavelengths. Fig. 6 shows a ratio map of the data. This was made by first smoothing the 850-μm data with 450-μm beam, and simultaneously smoothing the 450-μm data with

Downloaded from https://academic.oup.com/mnras/article/369/3/1201/1229160 by guest on 17 March 2021

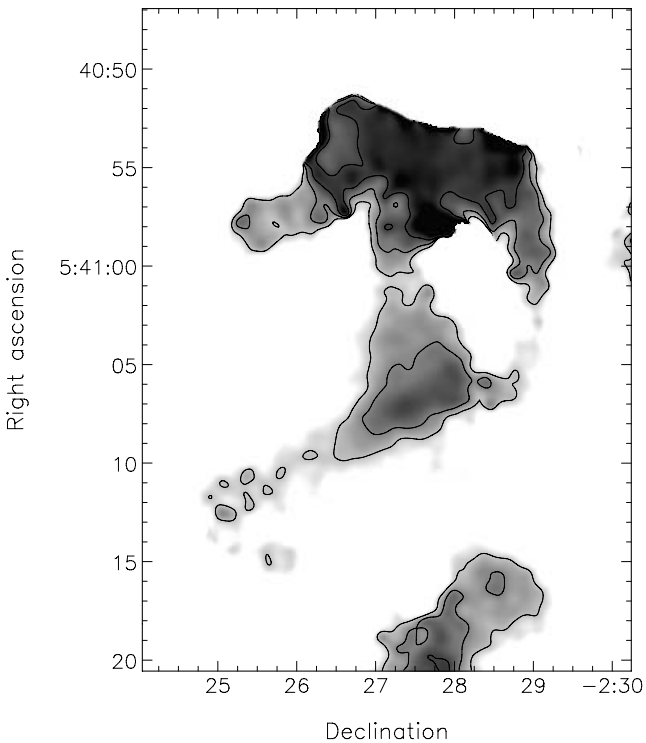

Figure 6. Image of the ratio of the 850- to 450-μm images shown in Figs 2 and 3 (after smoothing to a common resolution). Contour levels are 0.1, 0.2 and 0.3.

the 850-μm beam, then subtracting the background level from each map and dividing one by the other (after making a cut in the data to remove low-signal-to-noise-ratio regions of each map). It can be seen that the dust outside of the clumps SMM1 and 2 (that can be seen at high enough signal-to-noise ratio) has a ratio of 0.1–0.2 in this image. Higher values are seen towards the cores of SMM1 and 2. This is indicating a different spectral energy distribution for the two embedded sources relative to the less dense cloud. In addition, there is a difference between the two cores, such that the majority of SMM1 has a ratio of 0.3, while the majority of SMM2 has a ratio of 0.2.

The submillimetre spectral index $\alpha_{\rm SM}$ is usually defined as

$$\alpha_{\rm SM} = \frac{\log(S_{450}/S_{850})}{\log(\nu_{450}/\nu_{850})}, \tag{5}$$

where S_{450} and S_{850} are the flux densities at 450 and 850 μm respectively, and ν_{450} and ν_{850} are the frequencies at these wavelengths. A ratio of 0.1 in Fig. 6 corresponds to a submillimetre spectral index $\alpha_{\rm SM}$ of 3.6, while 0.2 corresponds to $\alpha_{\rm SM}$ of 2.6, and a ratio of 0.3 corresponds to $\alpha_{\rm SM}$ of 1.9. Values usually observed for dust in molecular clouds range from ∼2 to ∼4, as we see here.

Hence, we see that the dense sources have a lower value of $\alpha_{\rm SM}$ than the rest of the nebula. This could be caused by a lower temperature in the dense cores relative to the surrounding lower density cloud, such as is seen elsewhere in dense cores (Ward-Thompson et al. 2002). Furthermore, there is a marked difference between SMM1 and 2, with the former having a lower value for $\alpha_{\rm SM}$. This cannot be explained by temperature effects since SMM1 is warmer than SMM2 (see Section 3 above). It must be due to different dust properties in the two cores.

Recent work (Boudet et al. 2005) has shown that in the submillimetre regime there is an anticorrelation between the spectral index and the temperature, such that lower spectral indices are seen at higher temperatures. This work was based on studies carried out of the optical properties of amorphous silicate grains, but is in agreement with observations taken by the Programme National d'Observations Submillimetrique (PRONAOS) balloon-borne experiment (Lamarre et al. 1994; Lamarre & Giard 2002).

The variation of the spectral index seen by PRONAOS (Dupac et al. 2003) was ascribed to variations in the optical properties of amorphous silicate grains in different environments in the interstellar medium (Boudet et al. 2005). An alternative explanation in terms of dust grain coagulation was proposed by Stepnik et al. (2003). We are possibly seeing one of these effects here.

The Horsehead nebula is somewhat reminiscent of the Eagle nebula in appearance. In both cases columns of dense gas and dust 'point' towards H II regions where massive star formation has taken place. In the case of the Eagle nebula, dense clumps are seen at the tips of the columns (White et al. 1999). For the Horsehead nebula there is a dense region, SMM1, at the tip of the column (e.g. Abergel et al. 2003), and we see that there is another dense clump further 'down' the column, SMM2, apparently further from the ionizing radiation of the newly formed massive stars. We now discuss the possible formation mechanisms of SMM1 and 2.

In the Eagle nebula, White et al. (1999) argued that pre-existing clumps in the molecular cloud formed barriers to the ionizing winds from the massive stars in the H II region, and that the columns were essentially the 'wind shadows' of these clumps. In this picture, the clumps are eventually eroded by the massive stars, or else triggered into forming stars, in both cases meaning they are relatively short lived. Williams et al. (2001) presented an alternative scenario in which columns occur as natural instabilities in nature and can be quite long lived. For the Horsehead nebula, Pound et al. (2003) argued for a relatively short lifetime for the nebula.

Turning to our data, we see that SMM1 is clearly associated with the molecular cloud behind the PDR that is essentially the 'working surface' between the H II region and the cloud. The shape of the densest part of SMM1 is somewhat curved, as is the edge of the obscuration seen at the very 'top' of the horse's head in the optical image. If this curve were seen as an arc that formed part of a circle, then the centre of that circle would be somewhere in the vicinity of σ Ori, the star believed to be responsible for forming the PDR (Abergel et al. 2003). This appears to lend support to the hypothesis that SMM1 has been affected by its interaction with σ Ori.

SMM2 lies further 'down' the column of the Horsehead, and apparently further from σ Ori. It also appears to be being shielded by the remainder of the head and by SMM1. Hence it would appear that SMM2 may have been a pre-existing clump rather than a density enhancement caused by some form of 'snow-plough effect' (Elmegreen & Lada 1977). It is possible that the three-dimensional geometry of the nebula puts SMM2 slightly foreground to SMM1, and hence it is not shielded. In fact, in the optical image it is possible to discern a slightly brighter ridge roughly coincident with the 'top' of SMM2, so it may be that it is protruding somewhat from the near side of the cloud. However, there is no evidence for any significant PDR associated with this ridge.

5 STABILITY OF THE CONDENSATIONS

To determine whether the condensations in the Horsehead are prestellar (i.e. destined to spawn stars), we estimate the terms in the virial theorem, and present them in Table 3 (cf. Ward-Thompson 2002). For a spherical cloud to start contracting, the virial theorem

Downloaded from https://academic.oup.com/mnras/article/369/3/1201/1229160 by guest on 17 March 2021

Table 3. Terms in the virial theorem for the two clumps in the Horsehead (in units of 10^{42} erg). If the sum of the first three columns is greater than the sum of the final two, then the cloud will expand. If the sum of the last two columns is greater then the cloud will collapse.

Source	$2\mathcal{U}$	$2\mathcal{T}$	$2\mathcal{R}$	$\mathcal{G}$	$\mathcal{X}$
B33-SMM1	9	10	3	3	100
B33-SMM2	13	16	1	22	<20

requires that

$$2\mathcal{U} + 2\mathcal{T} + 2\mathcal{R} < \mathcal{G} + \mathcal{X}. \tag{6}$$

Here $\mathcal{U}$ is the thermal energy, $\mathcal{T}$ is the turbulent energy, $\mathcal{R}$ is the rotational energy, $\mathcal{G}$ is the magnitude of the self-gravitational potential energy and $\mathcal{X}$ is the contribution from external pressure ($\mathcal{X} = 4\pi R^3 P_{\rm EXT}$, where R is the cloud radius and $P_{\rm EXT}$ is the external pressure). Note that we have ignored the effects of any magnetic field that may be present in this region.

Twice the thermal energy is

$$2\mathcal{U} = \frac{3\,M\,k_{\rm B}\,T}{\bar{m}}, \tag{7}$$

where M is the total mass of the clump, T is its temperature, $\bar{m}$ is the mean molecular weight of the gas and $k_{\rm B}$ is the Boltzmann constant. We have assumed an isothermal gas which is effectively monatomic (since H_2 is not rotationally excited). Condensation B33-SMM1 is estimated to have mass $M \sim 2\,{\rm M}_\odot$ and temperature $T \sim 22$ K, giving $2\mathcal{U} \sim 9 \times 10^{42}$ erg. B33-SMM2 has $M \sim 4\,{\rm M}_\odot$ and $T \sim 15$ K, giving $2\mathcal{U} \sim 13 \times 10^{42}$ erg.

Twice the turbulent energy is

$$2\mathcal{T} = \frac{3\,M\,\Delta v^2_{\rm FWHM}}{8\,\ln(2)}, \tag{8}$$

where we have assumed isotropic turbulence, and $\Delta v_{\rm FWHM}$ is the FWHM of the radial velocity distribution (corrected for the thermal contribution). From the optically thin $C^{18}O$ ($2 \rightarrow 1$) line observations of Hily-Blant et al. (2005) we estimate $\Delta v_{\rm FWHM} \simeq 0.65\,{\rm km\,s^{-1}}$, and hence $2\mathcal{T} \sim 10 \times 10^{42}$ erg for B33-SMM1; and $\Delta v_{\rm FWHM} \simeq 0.6\,{\rm km\,s^{-1}}$, and hence $2\mathcal{T} \sim 16 \times 10^{42}$ erg for B33-SMM2.

Twice the rotational energy is

$$2\mathcal{R} = \frac{4\,M\,R^2\,\Omega^2}{5}, \tag{9}$$

where Ω is the angular rotational velocity of the clump. The values of Ω for SMM1 and 2 are estimated from fig. 8 of Hily-Blant et al. (2005). For B33-SMM1, we adopt $R \sim 0.1$ pc and $\Omega \simeq 3\,{\rm km\,s^{-1}\,pc^{-1}}$, giving $2\mathcal{R} \simeq 3 \times 10^{42}$ erg. For B33-SMM2, we adopt $R \sim 0.05$ pc and $\Omega \simeq 2\,{\rm km\,s^{-1}\,pc^{-1}}$, giving $2\mathcal{R} \simeq 1 \times 10^{42}$ erg.

The magnitude of the self-gravitational potential energy of a clump is given by

$$\mathcal{G} = \frac{\eta\,G\,M^2}{R}, \tag{10}$$

where η is a coefficient determined by the detailed density profile of the clump. If we assume that the clump is a critical Bonnor–Ebert sphere, which seems to be a good morphological approximation to many starless cores, then the coefficient, η, is given by

$$\eta = \left(\frac{3}{\xi\,\psi'} - \frac{{\rm e}^{-\psi}}{\psi'^2}\right)_{\rm B} = 0.732, \tag{11}$$

where $\psi(\xi)$ is the standard isothermal function (e.g. Chandrasekhar 1959), $\psi' \equiv {\rm d}\psi/{\rm d}\xi$, and the right-hand side is evaluated at the boundary of the critical solution (i.e. $\xi_{\rm B} \simeq 6.45$). Using the values of M and R cited above, we obtain $\mathcal{G} \sim 3 \times 10^{42}$ erg for B33-SMM1, and $\mathcal{G} \sim 22 \times 10^{42}$ erg for B33-SMM2.

To calculate the external pressure, we consider the flow of gas from a spherical globule which is being eroded by an ionization front. We assume that the gas flows away from the ionization front at constant speed equal to the speed of sound in the ionized gas, $a_{\rm II} \sim 10\,{\rm km\,s^{-1}}$. Consequently the density, $n_{\rm II}(r)$, in the ionized gas flowing off the globule is

$$n_{\rm II}(r) = n_{\rm II}(R)\left(\frac{r}{R}\right)^{-2}, \tag{12}$$

where r is radius measured from the centre of the globule, and $r = R$ is the boundary of the globule.

Since most of the ionizing photons incident on the globule will be used up maintaining ionization in the outflowing gas (rather than ionizing new gas), we can put

$$\frac{\dot{\mathcal{N}}_{\rm LyC}}{4\pi\,D^2} \simeq \int_{r=R}^{r=\infty} \alpha_\star\,n^2_{\rm II}(r)\,{\rm d}r \simeq \frac{\alpha_\star\,n^2_{\rm II}(R)\,R}{3}. \tag{13}$$

Here, $\dot{\mathcal{N}}_{\rm LyC}$ is the rate at which ionizing photons are emitted by the exciting star; for σ Ori, which is an O9.5 star, we adopt $\dot{\mathcal{N}}_{\rm LyC} \sim 3 \times 10^{48}\,{\rm s^{-1}}$ (Schaerer & de Koter 1997). D is the distance between the exciting star and the globule; we adopt the projected distances $D \sim 3.5$ pc for B33-SMM1, and $D \sim 3.8$ pc for B33-SMM2. $\alpha_\star \simeq 2 \times 10^{-13}\,{\rm cm^3\,s^{-1}}$ is the recombination coefficient for atomic hydrogen into excited states only – in accordance with the on-the-spot approximation – at the canonical temperature for the gas in an H II region, $T_{\rm II} \sim 10^4$ K. We note that in reality the outward flow of gas from the globule may be accelerated by the inward pressure gradient, but the integral in equation (13) is dominated by the region near the ionization front, and so this is unlikely to be a large correction.

From equation (13), we obtain

$$n_{\rm II}(R) \simeq \left(\frac{3\,\dot{\mathcal{N}}_{\rm LyC}}{4\pi\,D^2\,R\,\alpha_\star}\right)^{1/2}. \tag{14}$$

Hence, the pressure acting on the boundary of the globule, P_B, is given by

$$P_{\rm B} = 4\,n_{\rm II}(R)\,k_{\rm B}\,T_{\rm II}, \tag{15}$$

where there is a factor of 2 to allow for the contribution from electrons (assuming $n_{\rm e} \simeq n_{\rm p} \equiv n_{\rm II}$) and a factor of 2 to allow for the recoil of the ionized gas at speed $a_{\rm II}$. Since this pressure only acts on one side of the globule, we estimate the contribution to the virial theorem as

$$\mathcal{X} \simeq 2\pi\,R^3\,P_{\rm B} \sim \frac{4\,R^2\,k_{\rm B}\,T_{\rm II}}{D}\left(\frac{3\pi\dot{\mathcal{N}}_{\rm LyC}\,R}{\alpha_\star}\right)^{1/2}. \tag{16}$$

For B33-SMM1, we obtain $\mathcal{X} \sim 100 \times 10^{42}$ erg; and for B33-SMM2, $\mathcal{X} \lesssim 20 \times 10^{42}$ erg. We have not taken account of the shadowing effect of the nebula on SMM2 in this pressure term, hence it is quoted as an upper limit in Table 3.

We note that Habart et al. (2005) found an external pressure for SMM1 of $\sim 4 \times 10^6\,{\rm K\,cm^{-3}}$, which converts to a value of $\mathcal{X} \sim 85 \times 10^{42}$ erg in our terminology. This is in remarkably good agreement with our finding of $\mathcal{X} \sim 100 \times 10^{42}$ erg, using a completely different calculation. This independent check gives us further confidence in our calculated values.

Downloaded from https://academic.oup.com/mnras/article/369/3/1201/1229160 by guest on 17 March 2021

From the entries in Table 3, it appears that neither condensation is unequivocally bound if we look at the gravitational term alone. For SMM1 the left-hand side of equation (6) has a value of 22 (in units of 10^{42} erg) compared to a gravitational term of only 3. Hence, this is roughly an order of magnitude away from gravitational equilibrium. However, the pressure term has a value of 100, which would appear to tip the core very strongly in favour of collapse. We should be mindful that the external pressure only acts on one side of the condensation. Therefore, it may simply push the condensation along by the rocket effect (Kahn 1954; Oort & Spitzer 1955) rather than causing it to collapse, although the pressure from the rest of the cloud would tend to act to prevent this.

For SMM2, the left-hand side of equation (6) has a value of 30 (in units of 10^{42} erg) compared to a gravitational term of 22. These two values are remarkably similar, given the uncertainties in all of the above calculations. For example, an increase in the mass assumed for SMM2 of <20 per cent is all that is required make the two values equal. This is well within the uncertainties of our calculations, as discussed above. Therefore, we deduce that SMM2 is consistent with being in gravitational virial equilibrium, without any consideration of the external pressure.

This would appear to suggest that SMM2 was a pre-existing clump in B33 and is a candidate pre-stellar core (cf. Ward-Thompson et al. 2006). The external pressure term is quoted as an upper limit because we have not taken account of any shielding of SMM2 by the rest of the cloud. Nevertheless, if SMM1 is triggered to form stars, and the shock front and ionization front move further into the cloud, then the shielding would be removed and the full value quoted in Table 3 would be applicable. In that case we would say that SMM2 is also destined to collapse under the influence of the external pressure.

We re-iterate that inequality (6) is strictly only the condition for a clump to start contracting. Once contraction approaches freefall collapse, the non-thermal velocity dispersion has an increasing contribution from ordered inward motion, and therefore $\mathcal{T}$ as defined in equation (8) should be interpreted as the sum of the turbulent and bulk infalling energies, with the latter contribution becoming dominant. During collapse $\Delta\mathcal{T} \simeq \Delta\mathcal{G}$ and therefore quite quickly $2\mathcal{T} > \mathcal{G}$. Under this circumstance, the only way to confirm collapse is by measuring asymmetric line profiles. However, in the present case the fact that for SMM1 $2\mathcal{U} > \mathcal{G}$, and for SMM2 $2\mathcal{U} \sim \mathcal{G}$ suggests that neither clump is collapsing, yet.

We can estimate the speed, $-\dot{R}$, at which the shock front preceding the ionization front advances into each condensation, using conservation of mass across the ionization front:

$$-\dot{R} = \frac{n_{\rm II}(R)\, a_{\rm II}}{n(R)}; \tag{17}$$

and hence the time Δt it will take to ionize the whole of each existing condensation,

$$\Delta t \simeq \frac{\Delta Z}{-\dot{R}}, \tag{18}$$

where ΔZ is the distance to be travelled. In each case we took the shortest dimension, as we assumed that the cores are being flattened by the ionization front, causing them to lie parallel to it.

Combining equations (14), (17) and (18), we obtain $-\dot{R} \sim 0.3\,\mathrm{km\,s^{-1}}$ and $\Delta t \sim 0.4$ Myr for B33-SMM1; $-\dot{R} \sim 0.04\,\mathrm{km\,s^{-1}}$ and $\Delta t \sim 1.7$ Myr for B33-SMM2. However, these should be viewed as minimum lifetimes for the condensations, since they ignore the likelihood that the condensations are growing by sweeping up gas on the side opposite to the ionization front. None the less these values are consistent with the 5-Myr lifetime found for the entire nebula by Pound et al. (2003).

Hence, we find that SMM1 is being strongly affected by σ Ori and hence may be forced into some form of triggered collapse. On the other hand SMM2 appears to have been a pre-existing clump in the molecular cloud – possibly a pre-stellar core – which is in approximate gravitational virial equilibrium, but which may also eventually be forced into collapse by the external pressure from the H II region.

6 CONCLUSIONS

We have presented SCUBA images of the Horsehead nebula, B33, at 450 and 850 μm which show the familiar shape of the dust cloud responsible for the extinction in this famous nebula. We found strong emission coincident with the molecular cloud that borders the H II region at the 'top' of the horse's head, associated with the well-studied PDR in this region, which we labelled B33-SMM1. We calculated the physical parameters of this cloud and found that it contains a mass of $\sim 2\,\mathrm{M_\odot}$ in a region 0.31×0.13 pc. We also found the density in the heart of this region to be as high as $\sim 6 \times 10^5\,\mathrm{cm^{-3}}$, which is higher than had previously been seen. We calculated the virial balance of this clump, and found that the effect of the ionizing radiation from the nearby H II region has the strongest influence on its balance, such that it may subsequently undergo triggered star formation.

In addition, we found a source in the 'throat' of the horse that looks just as if it were a lump that the horse has swallowed. We labelled this source B33-SMM2. This source has not been previously well studied, and there appears to be no detection of emission from this source shortward of our 450-μm data. We calculated the mass and density of this source and found it has a mass of $\sim 4\,\mathrm{M_\odot}$ in a region 0.15×0.07 pc, with a peak density of $\sim 2 \times 10^6\,\mathrm{cm^{-3}}$. Based on our virial estimates for this core we found that SMM2 is in approximate gravitational equilibrium, consistent with it being a pre-stellar core that had already formed in B33, but that it may also eventually be triggered into collapse by the external H II region.

ACKNOWLEDGMENTS

The JCMT is operated by the Joint Astronomy Centre on behalf of the Particle Physics and Astronomy Research Council of the United Kingdom, the Netherlands Organization for Scientific Research and the National Research Council of Canada. SCUBA was built at the Royal Observatory, Edinburgh. The observations were carried out during the observing run with reference number M98BN06. ESO is acknowledged for permission to reproduce Fig. 1. DN acknowledges PPARC post-doctoral support and RA acknowledges PPARC studentship support that enabled them to work on this project. DW-T was on sabbatical at the Observatoire de Bordeaux whilst carrying out this work and gratefully acknowledges the hospitality accorded to him there. We also wish to thank Alain Abergel for providing us with the ISOCAM data.

REFERENCES

Abergel A. et al., 2003, A&A, 410, 577
André P., Ward-Thompson D., Barsony M., 1993, ApJ, 406, 122
André P., Ward-Thompson D., Motte F., 1996, A&A, 314, 625
Bacmann A., André P., Puget J.-L., Abergel A., Bontemps S., Ward-Thompson D., 2000, A&A, 361, 555
Barnard E. E., 1919, ApJ, 49, 1

Downloaded from https://academic.oup.com/mnras/article/369/3/1201/1229160 by guest on 17 March 2021

Boudet N., Mutschke H., Nayral C., Jäger C., Bernard J.-P., Henning T., Meny C., 2005, ApJ, 633, 272
Chandrasekhar S., 1959, An Introduction to Stellar Structure. Dover Press, New York
Dupac X. et al., 2003, A&A, 404, L11
Elmegreen B. G., Lada C. J., 1977, ApJ, 214, 725
Habart E., Abergel A., Walmsley C. M., Teyssier D., Pety J., 2005, A&A, 437, 177
Hily-Blant P., Teyssier D., Philipp S., Güsten R., 2005, A&A, 440, 909
Holland W. S. et al., 1999, MNRAS, 303, 659
Jenness T., Lightfoot J. F., 2000, Starlink User Note 216, Starlink Project, CCLRC, Chilton, UK
Johnstone D., Matthews H., Mitchell G. F., 2006, ApJ, 639, 259
Kahn F. D., 1954, BAIN, 12, 187
Kirk J. M., Ward-Thompson D., André A., 2005, MNRAS, 360, 1506
Lamarre J. M., Giard M., 2002, in Giard M., Bernard J.-P., Klotz A., Ristorcelli I., eds, ESA Publications Ser. Vol. 4, Infrared and Submillimeter Space Astronomy. ESA Publications Division, Noordwijk, p. 1
Lamarre J. M. et al., 1994, Infrared Phys., 35, 277
Nutter D. J., 2004, PhD thesis, Cardiff University, UK
Oort J. H., Spitzer L. Jr, 1955, ApJ, 121, 60
Pety J., Teyssier D., Fosse D., Gerin M., Roueff E., Abergel A., Habart E., Cernicharo J., 2005, A&A, 435, 885
Pound M. W., Reipurth B., Bally J., 2003, AJ, 125, 2108
Schaerer D., de Koter A., 1997, A&A, 322, 598
Stepnik B. et al., 2003, A&A, 398, 551
Teyssier D., Fossé D., Gerin M., Pety J., Abergel A., Roueff E., 2004, A&A, 417, 135
Ward-Thompson D., 2002, Sci, 295, 76
Ward-Thompson D., Scott P. F., Hills R. E., André P., 1994, MNRAS, 268, 276
Ward-Thompson D., Motte F., André P., 1999, MNRAS, 305, 143
Ward-Thompson D., André P., Kirk J. M., 2002, MNRAS, 329, 257
Ward-Thompson D., André P., Crutcher R. F., Johnstone D., Onishi T., Wilson C., 2006, Protostars and Planets V, in press
White G. J. et al., 1999, A&A, 342, 233
Williams R. J. R., Ward-Thompson D., Whitworth A. P., 2001, MNRAS, 327, 788

This paper has been typeset from a TEX/LATEX file prepared by the author.

Downloaded from https://academic.oup.com/mnras/article/369/3/1201/1229160 by guest on 17 March 2021